Journal of Materials Chemistry C

Carrier generation and compensation mechanism in $La_2SnO_2S_3$

Journal:	*Journal of Materials Chemistry C*
Manuscript ID	TC-ART-03-2024-001116.R1
Article Type:	Paper
Date Submitted by the Author:	08-Jun-2024
Complete List of Authors:	Nagafuji, Teruya; Tokyo Institute of Technology, Laboratory for Materials and Structures, Institute of Innovative Research Osuna, Koshiro; Tokyo Institute of Technology, Laboratory for Materials and Structures, Institute of Innovative Research Hanzawa, Kota; Tokyo Institute of Technology, Laboratory for Materials and Structures, Institute of Innovative Research Gake, Tomoya; Tokyo Institute of Technology, Laboratory for Materials and Structures, Institute of Innovative Research Bae, Soungmin; Tokyo Institute of Technology, Laboratory for Materials and Structures, Institute of Innovative Research Hu, Zhongxu; Tokyo Institute of Technology, MDX Research Center for Element Strategy, International Research Frontiers Initiative Katase, Takayoshi; Tokyo Institute of Technology - Suzukakedai Campus, MDX Research Center for Element Strategy, International Research Frontiers Initiative Takahashi, Akira; Tokyo Institute of Technology, Laboratory for Materials and Structures, Institute of Innovative Research Hiramatsu, Hidenori; Tokyo Institute of Technology, Laboratory for Materials and Structures, Institute of Innovative Research; Tokyo Institute of Technology, MDX Research Center for Element Strategy, International Research Frontiers Initiative Oba, Fumiyasu ; Tokyo Institute of Technology, Laboratory for Materials and Structures, Institute of Innovative Research; Tokyo Institute of Technology, MDX Research Center for Element Strategy, International Research Frontiers Initiative

Carrier generation and compensation mechanism in $La_2SnO_2S_3$

Teruya Nagafuji,[a] Koshiro Osuna,[a] Kota Hanzawa,[a] Tomoya Gake,[a] Soungmin Bae,[a] Zhongxu Hu,[b] Takayoshi Katase,[b] Akira Takahashi,[a] Hidenori Hiramatsu,*[ab] and Fumiyasu Oba **[ab]

[a] Laboratory for Materials and Structures, Institute of Innovative Research, Tokyo Institute of Technology, 4259 Nagatsuta, Midori-ku, Yokohama 226-8501, Japan

[b] MDX Research Center for Element Strategy, International Research Frontiers Initiative, Tokyo Institute of Technology, 4259 Nagatsuta, Midori-ku, Yokohama 226-8501, Japan

* Email: h-hirama@mces.titech.ac.jp

** Email: oba@msl.titech.ac.jp

Abstract

Some Cu-based oxychalcogenides demonstrate robust p-type conductivity while achieving effective n-type doping in such materials remains a persistent challenge. Among oxychalcogenides, $La_2SnO_2S_3$ has been proposed as a candidate for an n-type semiconductor because of its dispersive conduction band primarily derived from the Sn-5s states. The experimentally observed n-type conductivity of $La_2SnO_2S_3$ is, however, limited to a low value, and the underlying atomistic and electronic origins of this behavior remain unresolved. Our systematic first-principles calculations of its point defects using the Heyd–Scuseria–Ernzerhof hybrid functional indicate that the major source of carrier electrons in undoped $La_2SnO_2S_3$ is unintentionally incorporated H impurities rather than native defects. Moreover, the electrophilic behavior of $La_2SnO_2S_3$ is unveiled as a pivotal limiting factor for its n-type doping, where carrier electrons are readily trapped around Sn sites in the presence of S vacancies and interstitial H impurities, and even without these defects through self-trapping. This carrier-trapping mechanism is as significant as the electron compensation by Sn vacancies as major acceptor-type native defects. Our synthesis and characterization of polycrystalline $La_2SnO_2S_3$ confirm its moderate n-type conductivity and the presence of H impurities with a sizable concentration, both of which are in line with the theoretically predicted mechanism. These results clarify crucial limiting factors of n-type conductivity in $La_2SnO_2S_3$ and provide a fundamental guideline for the design of related n-type oxychalcogenides.

1 Introduction

Transparent conductive oxides play key roles in realizing modern applications such as flat-panel displays and solar cells.[1, 2] Many metal oxides exhibit wide band gaps, and most of them are known to be either insulators or n-type conductors.[3-8] As a prominent exception, $CuAlO_2$ was reported as a p-type transparent oxide by Kawazoe et al.[9] Its p-type conductivity was attributed to the Cu-3d character mixed with O-2p, which raises the top of the valence band compared with typical metal oxides, and the formation of native acceptors such as Cu vacancies.[10-12] This 'valance band component mixing' strategy has been extensively considered for designing p-type wide-gap oxides and oxychalcogenides.[13-21] Among them, LaCuO*Ch* (*Ch* = S, Se) was discovered as a derivative system of Cu-based oxides.[19, 20] The p-type conductivity has been reported for Mg-doped LaCuOS with a carrier density of 10^{20} cm^{-3}, but the mobility and electrical conductivity are quite low, ~0.2 $cm^2V^{-1}s^{-1}$ and ~5 Scm^{-1}, respectively.[22] A p-type Mg-doped LaCuOSe film has also been reported with a carrier density of 10^{21} cm^{-3}, a mobility of ~ 3.5 $cm^2V^{-1}s^{-1}$, and an electrical conductivity of ~ 910 Scm^{-1}.[21]

Increasing the carrier density through heavy doping typically degrades the carrier mobility owing to carrier scattering by dopants. The crystal structure of LaCuO*Ch*, which consists of an oxide layer (La_2O_2) and a chalcogenide layer (Cu_2Ch_2), is beneficial for circumventing such degradations because hole and electron conduction occurs mainly in the chalcogenide layer, while dopants can be chosen to selectively replace atoms in the oxide layer.[22, 23] If both p-type and n-type LaCuO*Ch* is available, its applications would be widened through the fabrication of *pn* homojunctions. However, the n-type doping of LaCuO*Ch* has not been realized so far. According to previous first-principles calculations, the low formation energy of the negatively charged Cu vacancy results in significant carrier electron compensation in LaCuOSe.[24, 25] $La_2CdO_2Se_2$ and $La_2SnO_2S_3$ without Cu components have also been explored as candidates for n-type wide-gap semiconductors.[18, 26, 27] The bottom of the conduction band in $La_2CdO_2Se_2$ consists mainly of the 5s-orbitals of Cd with a large spatial extent, which would be favorable for the n-type conduction.[26] Nevertheless, its n-type doping was found to be difficult.[26] Gake et al. investigated native point defects and dopants in $La_2CdO_2Se_2$ using first-principles calculations and suggested that negatively charged Cd vacancies substantially compensate carrier electrons,[28] as in the case of the Cu vacancies in LaCuO*Ch*.

Toward the understanding, design, and exploration of n-type oxychalcogenides, we here report a first-principles study of native point defects in $La_2SnO_2S_3$ to clarify the origin of experimentally observed low n-type conductivity. H impurities are also considered as they can be unintentionally incorporated during synthesis or intentionally chosen as effective dopants for electron doping. In addition to the electron compensation by the acceptor-type Sn vacancy, electron self-trapping around Sn sites is shown to play essential roles in regulating the n-type doping of $La_2SnO_2S_3$. The H impurities generate carrier electrons, but cause the Fermi level pinning below the conduction band minimum (CBM) by facilitating the electron trapping around nearby Sn sites. Such electron trapping is also enhanced by S vacancies. Given that available experimental reports on $La_2SnO_2S_3$ are rather limited,[18, 29, 30] we also experimentally revisit $La_2SnO_2S_3$ through the synthesis and characterization of polycrystalline samples. The results confirm the previously reported crystal structure, optical properties, and moderate n-type conduction behavior. In addition, a sizeable concentration of H impurities has been detected, in consistency with the theoretically predicted mechanisms of carrier generation and compensation.

2 Methods

2.1 Computational procedures

The first-principles calculations were performed using the projector augmented-wave method[31] and the Heyd–Scuseria–Ernzerhof (HSE06) hybrid functional [32, 33] as implemented in the VASP code.[34-36] PAW datasets with radial cutoffs of 1.48, 1.58, 0.80, 1.00, and 0.58 Å for La, Sn, O, S, and H, respectively, were employed, where La 5s, 5p, 5d, and 6s, Sn 5s and 5p, O 2s and 2p, S 3s and 3p, and H 1s were treated as valence electrons. The geometry of the primitive unit cell was optimized so that the residual stress and atomic forces became smaller than 0.01 GPa and 0.005 $eVÅ^{-1}$, respectively. A non-Γ-centered 2×2×1 *k*-point mesh and a plane-wave cut-off energy of 520 eV were used for the geometry optimization. The band structure, density of states (DOS), and complex dielectric function within the independent particle approximation[37] were calculated for the optimized structure using a plane-wave cut-off energy of 400 eV. The seekpath code,[38] which relies on the symmetry search using the spglib code,[39] was used to determine the band path. An absorption spectrum was derived from the calculated complex dielectric function. The band-averaged effective mass tensors for carrier electrons and holes were calculated using the BoltzTraP2 code,[40] where the carrier density and temperature were set to 10^{16} cm^{-3} and 300 K, respectively. A Γ-centered 6×6×2 *k*-point mesh was employed for the DOS, dielectric function, and effective mass calculations. The input files for these calculations were generated using the vise code.[41]

The vacancies (V_{La}, V_{Sn}, V_O, and V_S), the cation antisites (La_{Sn} and Sn_{La}), and the interstitials (La_i, Sn_i, O_i, and S_i) were considered in the native defect calculations. Here, the type of defects is denoted by X_Y, where X is the vacancy (V) or element and Y indicates a substitutional or interstitial (i) site. The antisite defect between a cation (La or Sn) and an anion (O or S), and that between O and S were excluded since the large charge and/or size mismatches would result in high formation energies. Among the native defects, V_{Sn}, V_O, V_S, and Sn_i with relatively low formation energies were selected based on the results of preliminary defect calculations using the Perdew–Burke–Ernzerhof functional tuned for solids (PBEsol);[42] see Fig. S1 in the ESI. These four kinds of native defects in relevant charge states were investigated using the HSE06 hybrid functional. In addition, H impurities were considered at various sites (H_O, H_S, and H_i). To model the native defects and H impurities, 128-atom supercells were constructed by the 2×2×1 expansion of the primitive cell. The positions with the lowest and the second lowest all-electron charge density in the perfect crystal were extracted using the pymatgen code[43] and adopted as the interstitial sites for the native defect species. Local minima of the electrostatic potential and local maxima of the electron localization function were considered as candidates for interstitial proton sites, and local minima of the charge density as candidates for interstitial hydride-ion sites.[44] The atoms adjacent to defects were randomly displaced by up to 0.2 Å in the initial supercell geometries to avoid symmetry-induced constraints in atomic relaxation. The all atomic positions were relaxed with the lattice parameters fixed at the optimized values for the perfect crystal. An atomic force convergence criterion of 0.03 eV $Å^{-1}$, a plane-wave cut-off energy of 400 eV, and a non-Γ-centered 2×2×1 *k*-point mesh were used in the defect calculations with spin polarization considered.

The formation energy of defect D in charge state q (D^q) is expressed as[45, 46]

$$E_\mathrm{f}[D^q] = E[D^q] + E_\mathrm{corr}[D^q] - E_\mathrm{p} - \sum_i \Delta n_i \mu_i + q(\varepsilon_\mathrm{VBM} + \Delta\varepsilon_\mathrm{F}), \qquad (1)$$

where $E[D^q]$ is the total energy of the supercell containing defect D^q and E_p is that of the corresponding perfect-crystal supercell. Δn_i is the difference in the number of i-type atoms (i = La, Sn, O, S, or H) between the defect and perfect-crystal supercells. μ_i denotes the chemical potential of the i-type atom. ε_VBM is the energy level of the valence band maximum (VBM), and $\Delta\varepsilon_\mathrm{F}$ is the Fermi level measured from ε_VBM. $E_\mathrm{corr}[D^q]$ is a finite-size correction term for $E[D^q]$ associated with artificial electrostatic interactions in charged defect supercells under three-dimensional periodic boundary conditions. The extended Freysoldt–Neugebauer–Van de Walle scheme was used for evaluating $E_\mathrm{corr}[D^q]$, where the anisotropic electrostatic screening effects were taken into account.[47, 48] The static dielectric tensor to describe the electrostatic screening is expressed as the sum of the vacuum permittivity and the electronic contribution (ε^ele) plus the ionic contribution (ε^ion). The finite-electric-field[49] and finite-displacement approaches were adopted to evaluate ε^ele and ε^ion, respectively, with a plane-wave cut-off energy of 400 eV and a non-Γ-centered 6×6×2 *k*-point mesh. The components of the calculated dielectric tensor are shown later. The pydefect code[41] was used to handle and analyze the defect calculations.

The chemical potential values within the single-phase region of $La_2SnO_2S_3$ are relevant to the defect energetics under the thermodynamic equilibrium. Therefore, the chemical potential diagram of the La–Sn–O–S quaternary system was constructed at 0 K and 0 Pa using the calculated total energies of relevant phases. The competing phases consisting of one to four elements from La, Sn, O, and S were selected from the Materials Project database[50] using a criterion of energy above hull less than 0.05 meV $atom^{-1}$. The La–Sn–O–S–H quinary system was similarly treated when H impurities in $La_2SnO_2S_3$ were considered. The standard states of the chemical potentials were set to the La, Cu, and S crystals and the O_2 and H_2 molecules. The crystalline phases were treated using the respective primitive cells, while the O_2 and H_2 molecules were modeled using cubic cells with a dimension of 10

Å each. Hereafter, the values of the chemical potentials will be expressed relative to those in the standard states as $\Delta\mu_i$.

2.2 Synthesis of polycrystalline $La_2SnO_2S_3$ samples

Commercially available reagent powders of La_2O_3 (Kojundo Chemical Lab. Co., Ltd., 99.9 %), La_2S_3 (Kojundo Chemical Lab. Co. Ltd., 99.9 %), and SnS_2 (Kojundo Chemical Lab. Co. Ltd., 99.9 %up) were employed for the synthesis of polycrystalline samples of $La_2SnO_2S_3$. Prior to the solid-phase reaction, La_2O_3 and La_2S_3 reagents were purified to remove impurities ($La(OH)_3$ in La_2O_3 and La_2O_2S in La_2S_3), because a three-phase mixed sample composed of $La_2SnO_2S_3$ (the main phase), La_2O_2S, and $La_2Sn_2O_7$ was obtained instead of the $La_2SnO_2S_3$ single phase when we did not carry out the purification. La_2O_3 reagent was subjected to dehydration at 1000 °C for 24 hours in ambient air, followed by thermal quench in a vacuum atmosphere. La_2S_3 reagent was thermally annealed at 1000 °C for 3 hours under a CS_2 flow condition, in which Ar was used as a carrier gas. SnS_2 reagent was confirmed as a single phase.

The purified La_2O_3 and La_2S_3 powders and SnS_2 reagent powder were stoichiometrically wet-mixed using a super-dehydrated heptane in an Ar-filled glove box (dew point < –100 °C, oxygen concentration < 0.1 ppm). The mixture was pressed into a disk, and then heated at 1000 °C for 12 hours in an evacuated silica-glass ampule.

2.3 Characterization

The crystalline phase and crystal structure were analyzed by powder X-ray diffraction (XRD) measurement at room temperature in ambient air with the Bragg-Brentano geometry using a Cu Kα radiation source. The calculation of the lattice parameters and Rietveld analysis were performed by a whole powder pattern fitting method using the SmartLab Studio II software (Rigaku Co., Japan).

A diffuse reflectance (R) spectrum was measured in ambient air at room temperature in the ultraviolet–visible wavelength (λ) region to estimate the optical band gap of $La_2SnO_2S_3$. The observed R spectrum was converted using the Kubelka–Munk function,

$$\alpha/s = (1 - R)^2/(2R), \tag{2}$$

where α and s denote the optical absorption coefficient and scattering factor, respectively. Using the α/s spectrum, the relationship between $(\alpha h\nu/s)^2$ and $h\nu$ was plotted for the direct transition, where h and ν are the Planck constant and frequency, respectively.

The thermal desorption spectroscopy (TDS) measurement for H_2 ($m/z = 2$) was implemented under a vacuum to determine the H impurity concentration in the $La_2SnO_2S_3$ powder. We transferred the powder sample from the Ar-filled glove box to the TDS measurement chamber without air exposure to precisely determine the H concentration in the inside bulk region, avoiding surface adsorption of air-related species such as moisture.

The electrical resistivity was examined by the four-probe method at room temperature in ambient air. Thermoelectric motive force under several temperature differences was measured at 40 °C in an He atmosphere to calculate a Seebeck coefficient and determine carrier polarity. Both measurements were conducted using sputtered gold electrodes as an ohmic contact.

3 Results and discussion

3.1 Crystal structure and fundamental properties

Fig. 1 shows the crystal structure of orthorhombic $La_2SnO_2S_3$ with a space group of *Pbnm* (No. 62) as reported experimentally. [30] It is characterized by alternating La_2O_2 and SnS_3 layers. The theoretical lattice parameters are compared with the present and previously reported experimental values[30] in Table 1; the details of the present experimental structural parameters are discussed in Section 3.3. The theoretical lattice parameters agree with both sets of the experimental values within 0.8% differences.

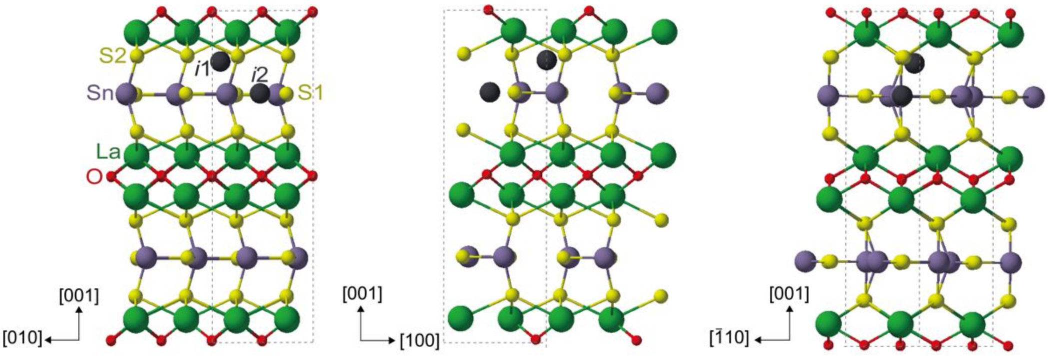

Fig. 1 Crystal structure of $La_2SnO_2S_3$ viewed from three directions. The frame indicates the unit cell. The black spheres denote two interstitial sites *i*1 and *i*2 considered as the initial positions of the interstitials in the native defect calculations.

Table 1 Lattice parameters (*a*, *b*, and *c*) and band gap (E_g) of $La_2SnO_2S_3$ from first-principles calculations compared with the present and reported experimental values.

	a (Å)	*b* (Å)	*c* (Å)	E_g (eV)
Theoretical	5.86	5.87	19.15	2.93
Experimental	5.862*	5.875*	19.07*	3[18]
	5.841[30]	5.851[30]	19.003[30]	

*This work: See Section 3.3 for details.

Fig. 2 shows the band structure, the total and projected DOSs, and the absorption spectrum for $La_2SnO_2S_3$. Both VBM and CBM are located at the Γ point, indicating the direct-type band structure. The calculated band gap of 2.93 eV is close to the reported experimental value of ~3 eV[18] as listed in Table 1. The valence band has a width of ~5 eV and its upper and middle parts consist mainly of S p-orbitals and O p-orbitals, respectively. The main components of the lower part of the valence band around −4 eV are Sn and S p-orbitals with a hybridization of O p-orbitals. The CBM is mainly constructed by Sn s-orbitals, which are hybridized with Sn and S p-orbitals. These features in the DOS indicate that the band gap of $La_2SnO_2S_3$ is mainly determined by the SnS_3 layer. The absorption spectrum shows a sharp onset around a photon energy of ~2.9 eV, corresponding to the direct band gap value.

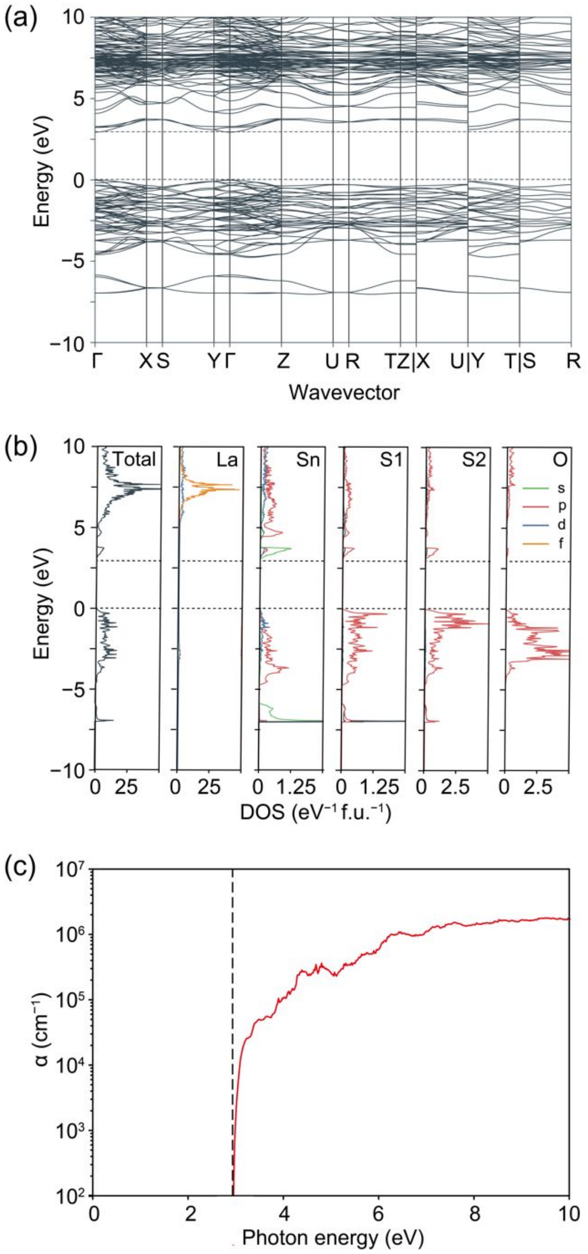

Fig. 2 (a) Band structure, (b) total DOS and the DOS projected on local orbitals at the respective atomic sites, and (c) absorption coefficient *α* as a function of the photon energy for $La_2SnO_2S_3$ from first-principles calculations. The dashed line indicates the photon energy corresponding to the band gap value.

The calculated band-averaged effective masses of $La_2SnO_2S_3$ are listed in Table 2. Despite the layered structure, the anisotropy in the effective masses is small, and the values perpendicular to the La_2O_2 and SnS_3 layers (*zz*) are even slightly lower than those in the parallel direction for both electron and hole masses. This is in contrast to the case of another non-Cu-based oxychalcogenide, $La_2CdO_2Se_2$, where the hole effective mass in the direction perpendicular to the constituent La_2O_2 and $CdSe_2$ layers is about 5 times higher than that in the parallel direction.[28] Electronic states near the VBM predominantly consist of Se *p*-orbitals in $La_2CdO_2Se_2$, while a sizable hybridization of the O *p*-orbital component is recognized for $La_2SnO_2S_3$ in Fig. 2b. This hybridization is associated with orbital interactions between the La_2O_2 and SnS_3 layers in $La_2SnO_2S_3$, which is expected to reduce the hole effective mass in the direction perpendicular to the layers. Moreover, both electron and hole effective masses are moderately low for $La_2SnO_2S_3$, considering the previously reported values of related wide-gap oxide and oxyselenide semiconductors from similar calculations: for instance, m_e^*/m_0 (*xx*) of 0.16 and m_e^*/m_0 (*zz*) of 0.17 for SnO_2[51] as an n-type semiconductor, m_h^*/m_0 (*xx*) of 1.93[12] and 1.92[51] and m_h^*/m_0 (*zz*) of 5.52[12] and 5.22[51] for $CuAlO_2$, and m_h^*/m_0 (*xx*) of 0.63 and m_h^*/m_0 (*zz*) of 2.83 for LaCuOSe [51] as p-type semiconductors.

Table 2 Electron (m_e^*) and hole (m_h^*) effective masses, and electronic (ε^{ele}) and ionic (ε^{ion}) contributions to dielectric tensor of $La_2SnO_2S_3$ from first-principles calculations. m_0 denotes the free-electron rest mass. ε^{ele} includes vacuum permittivity.

	xx	*yy*	*zz*
m_e^*/m_0	0.60	0.54	0.38
m_h^*/m_0	1.24	1.58	1.02
ε^{ele}	5.01	5.29	5.49
ε^{ion}	10.71	11.54	21.24

3.2 Defect formation energies and thermodynamic transition levels

We consider representative chemical potential conditions to discuss the energetics of the native defects and the H impurities. In the chemical potential diagram for the La–Sn–O–S–H quinary system, we found twenty-three chemical potential limits where $La_2SnO_2S_3$ exists in the single phase. The chemical potential values at respective limits and the competing phases are summarized in Table S1 (ESI). Note that these limits correspond to the solubility limits of H impurities. To obtain insight into the native defect formation and dopability of $La_2SnO_2S_3$, two chemical potential limits are selected: one where the La, Sn, and H chemical potentials are maximized and the O and S chemical potentials are minimized [$\Delta\mu_{La} = -5.25$, $\Delta\mu_{Sn} = -0.32$, $\Delta\mu_O = -2.90$, $\Delta\mu_S = -0.52$, and $\Delta\mu_H = 0$ (eV)] and the other where the La, Sn, and H chemical potentials are minimized, and the O and S chemical potentials are maximized [$\Delta\mu_{La} = -6.15$, $\Delta\mu_{Sn} = -1.22$, $\Delta\mu_O = -2.32$, $\Delta\mu_S = 0$, and $\Delta\mu_H = -0.21$ (eV)], both within the solubility limits of H. Hereafter, we call the former and latter the cation-rich and anion-rich conditions, respectively. We found that the chemical potential values of the host constituent atoms do not change under these representative conditions when we consider the La–Sn–O–S quaternary system without H (See Table S2 in the ESI). Therefore, the native defects and H impurities are discussed together under the aforementioned chemical potential conditions based on the quinary system.

Fig. 3 shows the formation energies of the selected native defects and the interstitial H impurity in $La_2SnO_2S_3$ under the cation-rich and anion-rich chemical potential conditions. In general, the positive and negative charge states of defects indicate their donor and acceptor behaviors, respectively. Under both chemical potential conditions, positively charged native defects exhibit relatively high formation energies and they are less stable than the negative charge states when the Fermi level is high. These results imply that none of the native defects are major sources of carrier electrons in $La_2SnO_2S_3$. On the contrary, the interstitial H impurity exhibits a positive charge state and a low formation energy in a wide Fermi level range; therefore, it can be a major donor. However, the negative charge state becomes energetically more favorable when the Fermi level is higher than ~2.4 eV, implying its carrier compensation behavior. This issue is detailed below.

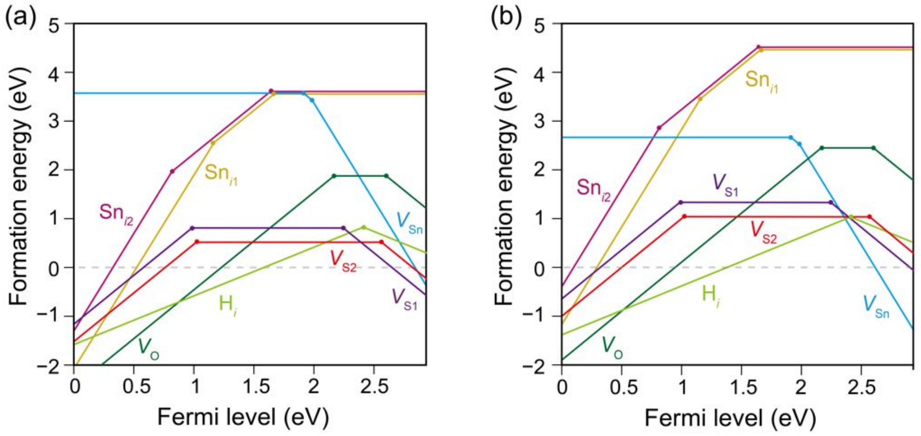

Fig. 3 Formation energies of major native defects and H impurities in $La_2SnO_2S_3$ as a function of the Fermi level obtained using first-principles calculations. (a) The cation-rich and (b) the anion-rich chemical potential conditions. The type of defect is denoted as X_Y, where X is the vacancy (V) or element, and Y indicates a substitutional or interstitial (i) site. The lower and upper limits of the Fermi level are taken to be the VBM and the CBM, respectively. Only defect formation energy in the energetically most favorable charge state is shown at a given Fermi level position, where the slope of the line corresponds to the defect charge state as given by eq 1. The filled circles denote thermodynamic transition levels between the energetically most favorable charge states; their positions are listed in Table S3 (ESI).

Among the possible range of the chemical potentials, the formation energy of H_i^+, which is likely to be a major source of carrier electrons, is minimized and that of V_{Sn}^{4-}, which is one of the main sources of electron compensation due to its acceptor nature, is maximized under the cation-rich conditions (Fig. 3a). Therefore, these chemical potential conditions are considered suitable for n-type doping of $La_2SnO_2S_3$ at first sight; the suppression of the electron compensation by acceptor-type defects is required even in n-type doping using other extrinsic donors. However, we found that the formation of the self-trapped electron $(\mathrm{e}_{\mathrm{ST}}^-)$ leads to a more complicated situation. In particular, the trapping of two electrons, which is denoted as $(2\mathrm{e})_{\mathrm{ST}}^{2-}$ hereafter, becomes stable (negative formation energy) when the Fermi level is located at 0.2 eV below the CBM or higher, as shown in Fig. 4a. The two-electron trapping occurs around an Sn site (Fig. 4b). This behavior is understandable in view of the fact that Sn takes multiple oxidation states of +2 and +4; specifically, the reduction from +4 to +2 occurs by the two-electron trapping in the present case. Moreover, we found that major donor-type defects (V_{S1} and H_i) facilitate electron trapping around nearby Sn sites (Figs. 4c and 4d); see Table 3 for the association energies. As a result, these defects show negative charge states when the Fermi level is close to the CBM. The − charge state of H_i is considered a proton plus $(2\mathrm{e})_{\mathrm{ST}}^{2-}$, rather than a hydride ion (Fig. 4d). For V_{S2} and V_{O}, we found that electrons are not necessarily localized around a single Sn site, but can be distributed into a few Sn sites and/or vacancy sites. Even some of the neutral vacancies show electron localization around Sn sites, rather than the vacancy sites, as previously found in amorphous SnO_2. [52]

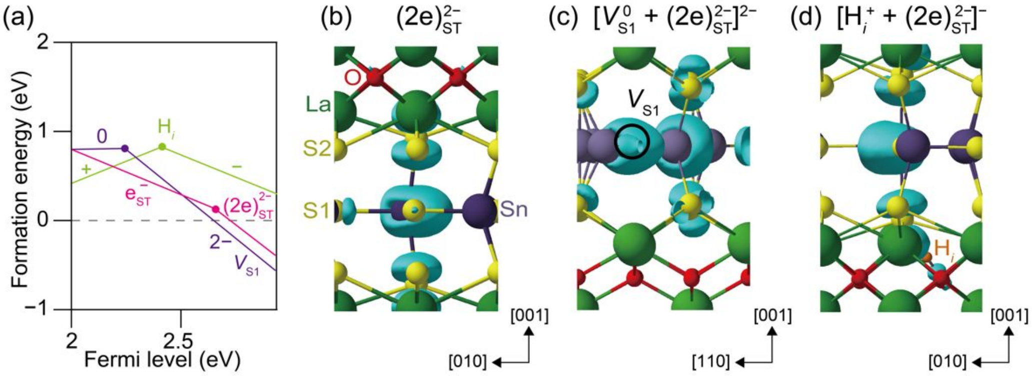

Fig. 4 (a) Formation energies of $\mathrm{e}_{\mathrm{ST}}^-$ and $(2\mathrm{e})_{\mathrm{ST}}^{2-}$ alongside those of V_{S1} and H_i in $La_2SnO_2S_3$ under the cation-rich chemical potential conditions obtained using first-principles calculations. Relaxed atomic configurations and the isosurfaces of the sum of the squared wave functions for two representative in-gap, occupied one-electron states for (b) $(2\mathrm{e})_{\mathrm{ST}}^{2-}$, (c) $[V_{\mathrm{S1}}^0 + (2\mathrm{e})_{\mathrm{ST}}^{2-}]^{2-}$ $(= V_{\mathrm{S1}}^{2-})$, and (d) $[\mathrm{H}_i^+ + (2\mathrm{e})_{\mathrm{ST}}^{2-}]^-$ $(= \mathrm{H}_i^-)$ in $La_2SnO_2S_3$. The blue isosurfaces correspond to 30% of the respective maximum values.

Table 3 Total energy change (ΔE) by the association between the S vacancy at the S1 site or the interstitial H impurity and self-trapped two electrons in $La_2SnO_2S_3$ from first-principles calculations. A negative ΔE value corresponds to an energy gain by association.

	ΔE (eV)
$V_{\mathrm{S1}}^{0} + (2\mathrm{e})_{\mathrm{ST}}^{2-} \rightarrow \left[V_{\mathrm{S1}}^{0} + (2\mathrm{e})_{\mathrm{ST}}^{2-}\right]^{2-} \left(= V_{\mathrm{S1}}^{2-}\right)$	−0.96
$\mathrm{H}_{i}^{+} + (2\mathrm{e})_{\mathrm{ST}}^{2-} \rightarrow \left[\mathrm{H}_{i}^{+} + (2\mathrm{e})_{\mathrm{ST}}^{2-}\right]^{-} \left(= \mathrm{H}_{i}^{-}\right)$	−0.63

The formation energy of $\left[V_{\mathrm{S1}}^{0} + (2\mathrm{e})_{\mathrm{ST}}^{2-}\right]^{2-} \left(= V_{\mathrm{S1}}^{2-}\right)$ is the lowest among these defects at a high Fermi level under the cation-rich conditions considered in Figs. 3a and 4a. Hence, it is likely that this defect mainly compensates carrier electrons and regulates the n-type doping of $La_2SnO_2S_3$.

Under the anion-rich conditions (Fig. 3b), the formation energy of the H interstitial remains low as the H chemical potential does not so much differ from the cation-rich conditions as mentioned above. In contrast, the formation energy of $\left[V_{\mathrm{S1}}^{0} + (2\mathrm{e})_{\mathrm{ST}}^{2-}\right]^{2-} \left(= V_{\mathrm{S1}}^{2-}\right)$ is clearly raised and that of V_{Sn}^{4-} is substantially lowered. Therefore, the compensation of carrier electrons by $\left[V_{\mathrm{S1}}^{0} + (2\mathrm{e})_{\mathrm{ST}}^{2-}\right]^{2-} \left(= V_{\mathrm{S1}}^{2-}\right)$ is relatively suppressed, but V_{Sn}^{4-} can be the main source of the carrier compensation, regulating the n-type doping of $La_2SnO_2S_3$. There would be optimum chemical potential conditions between the two limits where the formation of $\left[V_{\mathrm{S1}}^{0} + (2\mathrm{e})_{\mathrm{ST}}^{2-}\right]^{2-} \left(= V_{\mathrm{S1}}^{2-}\right)$ and V_{Sn}^{4-} is well balanced.

While we focus on the n-type dopability of $La_2SnO_2S_3$ in this study, the defect energetics based on Fig. 3 also provides insights into its p-type doping. The major donor-type native defects show low, negative formation energies when the Fermi level is close to the VBM under both chemical potential conditions. Therefore, holes are severely compensated even when introduced by acceptor dopants, indicating that the p-type doping of $La_2SnO_2S_3$ is unfeasible.

In summary, H_{i}^{+} is stable over a wide range of the Fermi level and the formation energy is relatively low under both cation-rich and anion-rich conditions. It is likely to act as the main source of carrier electrons in $La_2SnO_2S_3$, given that there is no native defect with comparable characteristics. However, the H impurity facilitates electron trapping around a nearby Sn site when the Fermi level is close to the CBM. Thus, the electron self-trapping, which is an intrinsic behavior of $La_2SnO_2S_3$, and that enhanced by the H impurity and the S vacancy restrict the increase in the carrier electron density.

3.3 Experimental revisit to the crystal, optical, and electrical properties of $La_2SnO_2S_3$

Fig. 5 shows an XRD profile of a polycrystalline $La_2SnO_2S_3$ sample. A single phase of $La_2SnO_2S_3$ has been obtained without detectable impurity phases. The result of the Rietveld analysis is shown in Fig. S2 (ESI), alongside the refined structural parameters (Tables S4 and S5 in the ESI; the crystallographic data after the Rietveld refinement can be obtained from CCDC 2322792). The orthorhombic crystal structure with a space group of *Pbnm* (No. 62) and structural parameters are consistent with the previously reported ones; [30] the lattice parameters determined using the present sample are compared with the reported values in Table 1.

From the R vs. λ spectrum shown in Fig. 6a, the optical band gap of $La_2SnO_2S_3$ is estimated to be ~3.0 eV, which is consistent with the previously reported value of ~3 eV.[18] However, a slightly smaller value of ~2.9 eV is estimated from the $(\alpha h\nu/s)^2$ vs. $h\nu$ plot that assumes the direct transition (Fig. 6b). Although one of the possible origins of this small energy difference is the presence of in-gap tail states originating from defects, a more accurate determination of the optical band gap is difficult only by a diffuse reflectance measurement on a polycrystalline powder sample. Thus, we conclude that the optical band gap of $La_2SnO_2S_3$ is 2.9 – 3.0 eV, which is consistent with the light-yellow color of the polycrystalline sample shown in the inset of Fig. 6a and the theoretical value of 2.9 eV. An experimental observation of the absorption spectrum of a high-quality thin-film sample would be required to determine the optical band gap more precisely.

As our first-principles calculations suggest that interstitial H impurities are relevant donors in $La_2SnO_2S_3$, we have carefully conducted the TDS analysis of our sample to quantify the H concentration. The resultant spectrum is shown in Fig. 7. Its analysis indicates that the sample includes H impurities with a concentration of 0.3 at%, corresponding to 2×10^{19} cm^{-3}. In addition, the low desorption temperature starting around 100 °C supports the existence of weakly bonded interstitial H impurities in $La_2SnO_2S_3$. The electrical resistivity and the Seebeck coefficient are estimated to be 1.1×10^6 Ωcm at room temperature (ca. 25 °C) and −13 mV K^{-1} at 40 °C, respectively, from the results of the current-voltage characteristic and thermoelectric motive force measurements shown in Fig. 8. The negative Seebeck coefficient indicates n-type behavior of the $La_2SnO_2S_3$ sample. Assuming electron mobilities of 0.1 to 10 cm^{2}V^{-1}s^{-1}, the carrier electron density is estimated to be 6×10^{11} to 6×10^{13} cm^{-3}. The low carrier density is consistent with the large Seebeck coefficient. The moderate n-type conductivity is similar to the behavior of a polycrystalline $La_2SnO_2S_3$ sample in a previous report,[18] in which H impurities may also be unintentionally incorporated with a sizeable concentration.

We have also attempted F and Cl doping, expecting that they substitute for O and S, respectively, and act as donors. However, no significant change was observed in the electrical resistivity, as in the case of the previously attempted Nb and Sb doping.[18] These results are consistent with the aforementioned mechanism based on the theoretical defect energetics, where the compensation by the acceptor-type Sn vacancy and the self-trapping limit the carrier electron density.

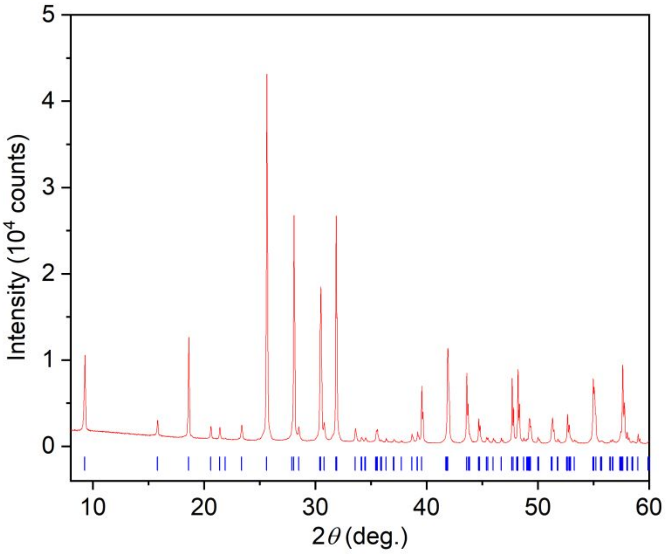

Fig. 5 XRD profile of a polycrystalline $La_2SnO_2S_3$ sample. The blue lines indicate the positions of the diffraction peaks.

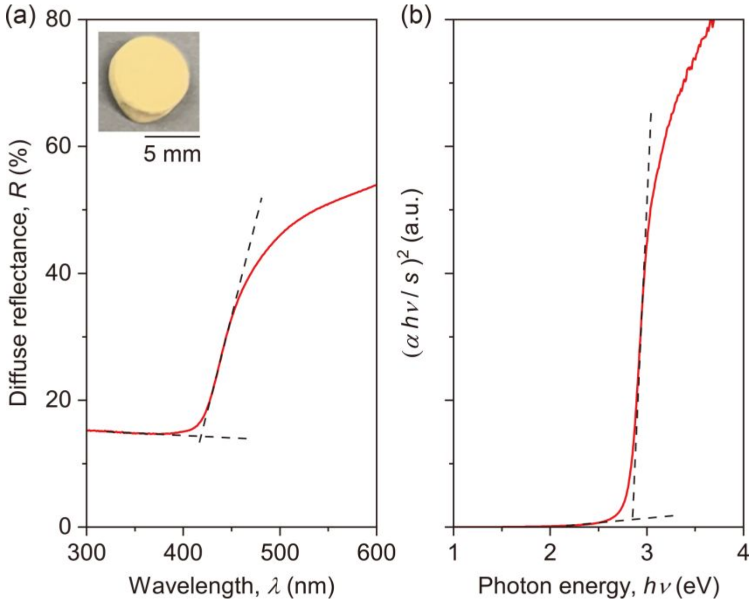

Fig. 6 Optical properties of a polycrystalline $La_2SnO_2S_3$ sample. (a) Diffuse reflectance spectrum. The inset shows an optical micrograph of the sample. (b) $(\alpha h\nu/s)^2$ vs. $h\nu$ plot. Dashed straight lines in (a) and (b) are used to estimate the optical band gap.

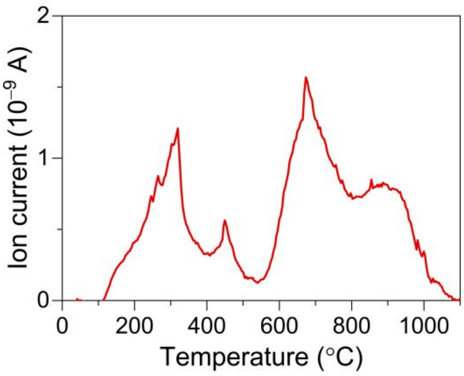

Fig. 7 TDS spectrum of hydrogen ($m/z = 2$) for a polycrystalline $La_2SnO_2S_3$ sample.

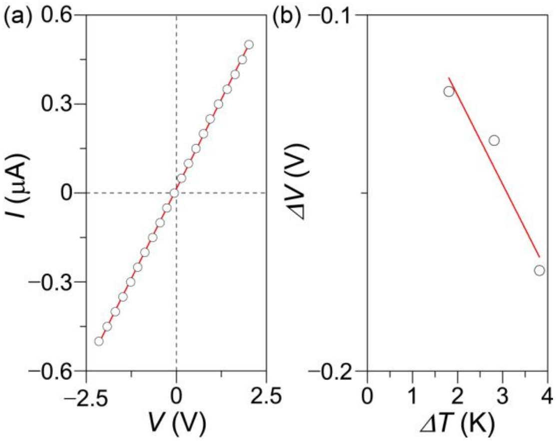

Fig. 8 Electrical properties of a polycrystalline $La_2SnO_2S_3$ sample. (a) Current (I)-voltage (V) characteristic at room temperature (ca. 25 °C) in air and (b) thermoelectric motive force (ΔV) as a function of temperature difference (ΔT) at 40 °C in an He atmosphere.

3.4 Relationship between crystal and electronic structures of $La_2SnO_2S_3$

The electronic structure around the band gap of $La_2SnO_2S_3$ is predominated by the SnS_3 layer, as shown in Section 3.1. We thus compare its crystal and local structures with those of simple binary tin sulfides, SnS_2 [53] and SnS, [54] and discuss the relationship with the electronic structures and electron trapping behavior. All the structural parameters considered here are summarized in Table S6 (ESI).

Fig. 9a shows the crystal structure of SnS_2. Six S atoms form a nearly perfect regular octahedron, in which the Sn atom occupies the 6-fold coordination center position (Fig. 9a, upper). These octahedra are edge-sharing along the *a*- and *b*-axes, and constructs a neutral $Sn_{0.5}S$ layer in the *ab*-plane (Fig. 9a, lower). The $Sn_{0.5}S$ layers are stacked along the *c*-axis and weakly bound by van der Waals interactions.

In the case of SnS, the coordination number of Sn is usually regarded as 3 (Fig. 9b, left). The SnS_3 polyhedron that is a component of the corner-sharing SnS layers possesses a trigonal pyramid geometry, which implies the existence of lone pair electrons from the viewpoints of the $(5s)^2$ formal electronic configuration and stereochemistry for divalent Sn. The SnS layers are stacked along the *a*-axis, which constitutes a layered structure as in the case of SnS_2. This Sn local structure in SnS can also be regarded as a 6-fold coordination when relatively distant three Sn–S pairs (3.29–3.39 Å) are assumed to form weak chemical bonds (Fig. 9b, right). The distorted SnS_6 octahedra are edge-sharing along the *b*- and *c*-axes. Because the Sn atom is located at an off-centered position in the octahedron, all S–Sn–S angles are far from the regular octahedron values of 90 and 180 degrees.

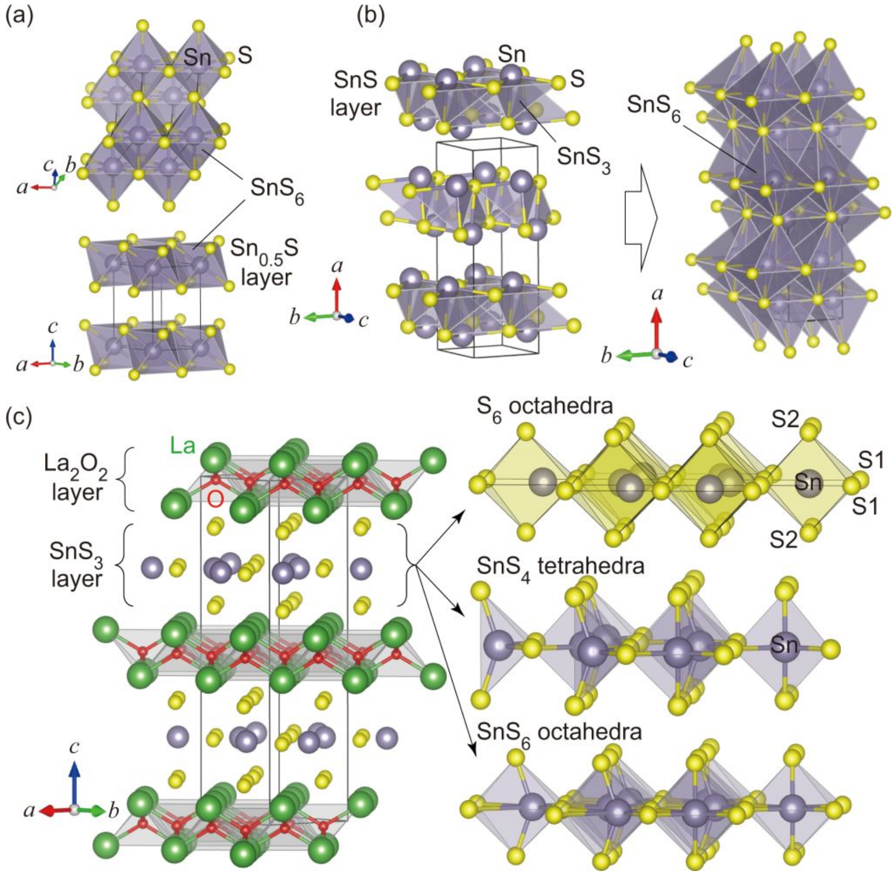

Fig. 9 Crystal structures of (a) SnS_2, (b) SnS, and (c) $La_2SnO_2S_3$. Two kinds of visual aspects are drawn by the same octahedra configuration in (a). The coordination number of Sn is modified from 3 to 6 in the right panel of (b). The atomic structures of the SnS_3 layer are described in three different ways in the right panel of (c). The VESTA code [55] was used for the visualization.

Based on the above interpretation of the crystal structures of the binary sulfides, we now view the structure of $La_2SnO_2S_3$ (Fig. 9c, left). Focusing on the SnS_3 layer, a quasi-square S1 lattice in the *ab*-plane and two apical S2 construct edge-sharing octahedra (Fig. 9c, right upper). This relatively isotropic and edge-sharing S_6 octahedral configuration is similar to SnS_2 possessing the same +4 formal charge of Sn. However, the most different point from SnS_2 is the Sn position, which is far from the center in the quasi-square S1 lattice. Accordingly, we may regard this local configuration as a SnS_4 tetrahedron including two in-plane S1 and two apical S2 (Fig. 9c, right middle), which is corner-sharing along the *b*-axis each other (see Fig. S3 in the ESI for the views from different directions). Because of the off-centered Sn position, all S–Sn–S angles are far from the regular tetrahedron value of 109.47 degrees. The bond lengths of Sn–S1 and Sn–S2 (2.31–2.49 Å) are clearly shorter than those of SnS with divalent Sn ($\geq$ 2.62 Å), implying that the effective charge of Sn in $La_2SnO_2S_3$ is higher than that in SnS, as expected from the formal charge of +4. In contrast, when relatively distant in-plane Sn–S1 pairs (3.43 and 3.45 Å) are regarded to form weak chemical bonds like the SnS case, we can also draw edge-sharing SnS_6 octahedra with off-centered Sn atoms (Fig. 9c, right lower). In this case, all S–Sn–S angles, as well as the variations in the Sn–S distance, are also far from those of the regular octahedron. It should be noted that this off-centered Sn octahedral structure resembles that of SnS, not SnS_2. This structural analogy with SnS composed of divalent Sn would explain why the two-electron trapping easily occurs in $La_2SnO_2S_3$ with formally tetravalent Sn. The intrinsically large open space around the off-centered Sn atoms in $La_2SnO_2S_3$ would readily accommodate two additional electrons that are localized like a lone pair around an Sn site. This consideration seems to be proper also in terms of stereochemistry.

It is well recognized that the binary chalcogenides of divalent Sn, SnS and SnSe, tend to be p-type, and strategies to convert them into n-type have been explored both experimentally and theoretically.[56-62] In contrast, undoped SnS_2 and $SnSe_2$ with tetravalent Sn have been reported to be n-type.[63-65] $La_2SnO_2S_3$ with tetravalent Sn follows this n-type tendency of the tetravalent Sn binary chalcogenides. However, the two-electron self-trapping mechanism proposed in this study may be intrinsic to $La_2SnO_2S_3$ having the SnS-like local structure.

The lower part of the conduction band of $La_2SnO_2S_3$ is dominated by the Sn 5s states as mentioned above. The first and second neighboring Sn–Sn distances (3.61 and 4.77 Å) are distributed in the *ab*-plane, and the directions of these neighboring Sn pairs are close to those of the diagonals (see Fig. S3 in the ESI for its plan view). Therefore, Sn 5s–Sn 5s interaction is expected to be almost isotropic in the *ab*-plane, leading to the nearly isotropic in-plane electron effective masses [m_e^*/m_0 $(xx) = 0.60$, m_e^*/m_0 $(yy) = 0.54$] in $La_2SnO_2S_3$. Additionally, three structural factors would be complicatedly related to the anisotropy of the electron effective masses between in-plane (*xx* and *yy*) and out-of-plane (*zz*): (i) the shortest Sn–S2 bond (2.31 Å, S2: the out-of-plane apical site) among Sn–S bonds, (ii) short O–La bonds (2.38–2.43 Å), and (iii) relatively short La–S distances (3.18–3.28

Å). For (i), the Sn–S2 bond is much shorter than in-plane Sn–S1 ones (2.49–3.45 Å) and the sum of each ionic radius: 0.55 Å (CN = 4, where CN denotes the coordination number) and 0.69 Å (CN = 6) for Sn^{4+}, and 1.84 Å (CN = 6) for S^{2-} according to Shannon's radii,[66] while Pauling's radius of S^{2-} is also 1.84 Å;[67] note that the CN of S looks 5 rather than 6 in $La_2SnO_2S_3$, which may affect the comparison with the ionic radii. For (ii), they are sufficiently shorter than the sum of each ionic radius, 1.16 Å for La^{3+} and 1.38 Å for O^{2-},[66] implying a significant covalency contribution. For (iii), most of them are shorter than that (3.25 Å) in the oxysulfide LaCuOS with a similar layered structure,[68] resulting in larger in-plane S–La–S angles (78–81 and 130 degrees) than those (76 and 121 degrees) in LaCuOS, and stronger interaction between La and S in $La_2SnO_2S_3$. These three factors would contribute to sizable orbital interactions in the out-of-plane direction, leading to the lower out-of-plane electron effective mass [m_e^*/m_0 (zz) = 0.38] than in-plane effective masses, despite the long out-of-plane Sn–Sn distance (9.74 Å) owing to the layered structure interposed by La_2O_2 layers. Accordingly, the electron effective masses of $La_2SnO_2S_3$ are more isotropic than similarly calculated values of SnS_2 with m_e^*/m_0 (xx) = 0.35 and m_e^*/m_0 (zz) = 0.96. Although the shortest in-plane Sn–Sn and Sn–S distances in $La_2SnO_2S_3$ are shorter than those in SnS_2, in-plane electron effective masses of $La_2SnO_2S_3$ are higher than that of SnS_2. It would be reasonable to consider that one of the origins is two distant in-plane Sn–S1 bonds (3.43 and 3.45 Å) out of six Sn–S bonds in $La_2SnO_2S_3$; i.e., they would cause totally weaker hybridization between Sn and S in $La_2SnO_2S_3$.

Finally, we briefly comment on a feature of the La_2O_2 layer. The local structure (O–La = 2.38–2.43 Å, La–O–La = 104–105 and 119–120 degrees) composed of edge-sharing La_4O tetrahedra (Fig. 9c, left) is quite similar to those in *ReMOCh* (*Re* = rare earth, La–Er; *M* = monovalent metal, Cu, Ag; *Ch* = chalcogen, S–Te), [69] $La_2CdO_2Se_2$, [26] $La_2ZnO_2Se_2$, [70], $LaGaOSe_2$, [71] and *ReTmOPn* (*Re* = La–Sm; *Tm* = 3d or 4d transition metal, Cr–Ni, Zn, Ru, Os; *Pn* = pnictogen, P–Sb), [69] all of which belong to an isomorphism-like layered structure of $La_2SnO_2S_3$; i.e., all of these quaternary oxychalcogenides and oxypnictides are composed of alternately stacked rare-earth oxide layers and chalcogenide/pnictide ones (Fig. S4 in the ESI). Therefore, the rare-earth oxide layer is regarded as a common building block of these mixed-anion compounds. However, it appears that the out-of-plane orbital interactions depend significantly on the composition and structure of the chalcogenide layer.

4 Conclusions

We have systematically investigated the bulk fundamental properties, native defects, H impurities, and electron self-trapping in $La_2SnO_2S_3$ using the HSE06 hybrid functional. The calculated structural parameters and band gap are well consistent with the previously reported and the present experimental values. The electronic states at the VBM and CBM of $La_2SnO_2S_3$ are formed primarily from S p-orbitals and Sn s-orbitals, respectively, indicating that the band gap of $La_2SnO_2S_3$ is mainly determined by the SnS_3 layer. Both electron and hole effective masses are moderately low and do not show significant anisotropy despite the layered structure.

From the theoretical formation energies of the major native defects, H impurities, and self-trapped electron(s), we found that H_i^+ can be the major source of carrier electrons, but also facilitate two-electron trapping around a nearby Sn site when the Fermi level is close to the CBM. Similarly, two-electron trapping enhanced by anion vacancies such as $\left[V_{\mathrm{S1}}^{0}+(2\mathrm{e})_{\mathrm{ST}}^{2-}\right]^{2-}\left(=V_{\mathrm{S1}}^{2-}\right)$, as well as the formation of the acceptor-type Sn vacancy, causes carrier compensation in $La_2SnO_2S_3$, regulating its n-type doping. The two-electron trapping behavior is explainable in terms of the relatively easy reduction of Sn from the +4 to +2 oxidation states and the local environment of the Sn site in $La_2SnO_2S_3$. These carrier generation and compensation mechanisms are consistent with the fact that $La_2SnO_2S_3$ shows a moderate n-type conductivity as found by the previous study[18] and the present experiment on polycrystalline $La_2SnO_2S_3$ samples, the latter of which has also detected a sizable concentration of H impurities.

Supplementary information

Electronic supplementary information (ESI) available. See DOI:

Conflicts of interest

There are no conflicts to declare.

Data availability statement

Crystallographic data for $La_2SnO_2S_3$ has been deposited at the CCDC under CCDC 2322792 and can be obtained free of charge via www.ccdc.cam.ac.uk/data_request/cif, or by emailing data_request@ccdc.cam.ac.uk, or by contacting The Cambridge Crystallographic Data Centre, 12 Union Road, Cambridge CB2 1EZ, UK; fax: +44 1223 336033.

Acknowledgements

This work was supported by JSPS KAKENHI Grant Numbers JP20H00302, JP20K15170, JP21H04612, JP22K14601, JP22H01766, JP22K18881, JP23KF0030, and JP24H00376, KISTEC Project, JST CREST Grant Number JPMJCR17J2, MEXT Data Creation and Utilization Type Material Research and Development Project Grant Number JPMXP1122683430, MEXT Collaborative Research Project of Laboratory for Materials and Structures, and MEXT Design and Engineering by Joint Inverse Innovation for Materials Architecture Project. The computing resources of the TSUBAME3.0 supercomputer at Tokyo Institute of Technology, the Academic Center for Computing and Media Studies at Kyoto University, and Research Institute for Information Technology at Kyushu University were used.

References

1. A. Facchetti and T. J. Marks, *John Wiley & Sons, Inc.*, 2010.
2. S. C. Dixon, D. O. Scanlon, C. J. Carmalt and I. P. Parkin, *J. Mater. Chem. C*, 2016, **4**, 6946-6961.
3. I. Hamberg and C. G. Granqvist, *J. Appl. Phys.*, 1986, **60**, R123-R160.
4. H. Ohta, M. Orita, M. Hirano, H. Tanji, H. Kawazoe and H. Hosono, *Appl. Phys. Lett.*, 2000, **76**, 2740-2742.
5. T. Ishida, O. Tabata, J. I. Park, S. H. Shin, H. Magara, S. Tamura, S. Mochizuki and T. Mihara, *Thin Solid Films*, 1996, **281-282**, 228-231.
6. H. S. Randhawa, M. D. Matthews and R. F. Bunshah, *Thin Solid Films*, 1981, **83**, 267-271.
7. R. Banerjee and D. Das, *Thin Solid Films*, 1987, **149**, 291-301.
8. T. Minami, H. Nanto and S. Takata, *Appl. Phys. Lett.*, 1982, **41**, 958-960.
9. H. Kawazoe, M. Yasukawa, H. Hyodo, M. Kurita, H. Yanagi and H. Hosono, *Nature*, 1997, **389**, 939-942.
10. X. Nie, S. H. Wei and S. B. Zhang, *Phys. Rev. Lett.*, 2002, **88**, 066405.
11. D. O. Scanlon and G. W. Watson, *J. Phys. Chem. Lett.*, 2010, **1**, 3195-3199.
12. T. Gake, Y. Kumagai, A. Takahashi and F. Oba, *Phys. Rev. Mater.*, 2021, **5**, 104602.
13. A. Kudo, H. Yanagi, H. Hosono and H. Kawazoe, *Appl. Phys. Lett.*, 1998, **73**, 220-222.
14. K. Ueda, T. Hase, H. Yanagi, H. Kawazoe, H. Hosono, H. Ohta, M. Orita and M. Hirano, *J. Appl. Phys.*, 2001, **89**, 1790-1793.
15. M. K. Jayaraj, A. D. Draeseke, J. Tate and A. W. Sleight, *Thin Solid Films*, 2001, **397**, 244-248.
16. H. Yanagi, T. Hase, S. Ibuki, K. Ueda and H. Hosono, *Appl. Phys. Lett.*, 2001, **78**, 1583-1585.
17. R. Nagarajan, A. D. Draeseke, A. W. Sleight and J. Tate, *J. Appl. Phys.*, 2001, **89**, 8022-8025.
18. K. Ueda, H. Hiramatsu, M. Hirano, T. Kamiya and H. Hosono, *Thin Solid Films*, 2006, **496**, 8-15.
19. K. Ueda, S. Inoue, S. Hirose, H. Kawazoe and H. Hosono, *Appl. Phys. Lett.*, 2000, **77**, 2701-2703.
20. H. Hiramatsu, K. Ueda, H. Ohta, M. Hirano, T. Kamiya and H. Hosono, *Appl. Phys. Lett.*, 2003, **82**, 1048-1050.
21. H. Hiramatsu, K. Ueda, H. Ohta, M. Hirano, M. Kikuchi, H. Yanagi, T. Kamiya and H. Hosono, *Appl. Phys. Lett.*, 2007, **91**, 012104.
22. H. Hiramatsu, H. Kamioka, K. Ueda, H. Ohta, T. Kamiya, M. Hirano and H. Hosono, *Phys. Status Solidi (a)*, 2006, **203**, 2800-2811.
23. K. Ueda and H. Hosono, *Thin Solid Films*, 2002, **411**, 115-118.
24. H. Hiramatsu, T. Kamiya, T. Tohei, E. Ikenaga, T. Mizoguchi, Y. Ikuhara, K. Kobayashi and H. Hosono, *J. Am. Chem. Soc.*, 2010, **132**, 15060-15067.

25. D. O. Scanlon, J. Buckeridge, C. R. A. Catlow and G. W. Watson, *J. Mater. Chem. C*, 2014, **2**, 3429-3438.

26. H. Hiramatsu, K. Ueda, T. Kamiya, H. Ohta, M. Hirano and H. Hosono, *J. Mater. Chem.*, 2004, **14**, 2946-2950.

27. H. Hiramatsu, K. Ueda, T. Kamiya, H. Ohta, M. Hirano and H. Hosono, *J. Phys. Chem. B*, 2004, **108**, 17344-17351.

28. T. Gake, Y. Kumagai, A. Takahashi, H. Hiramatsu and F. Oba, *J. Mater. Chem. C*, 2022, **10**, 16828-16837.

29. M. Guittard, S. Benazeth, J. Dugue´, S. Jaulmes, M. Palazzi, P. Laruelle and J. Flahaut, *J. Solid State Chem.*, 1984, **51**, 227-238.

30. S. Bénazeth, M. Guittard and P. Laruelle, *Acta Crystallogr. C Struct. Chem.*, 1985, **41**, 649-651.

31. P. E. Blöchl, *Phys. Rev. B Condens. Matter*, 1994, **50**, 17953-17979.

32. J. Heyd, G. E. Scuseria and M. Ernzerhof, *The Journal of Chemical Physics*, 2003, **118**, 8207-8215.

33. A. V. Krukau, O. A. Vydrov, A. F. Izmaylov and G. E. Scuseria, *J. Chem. Phys.*, 2006, **125**, 224106.

34. G. Kresse and J. Furthmüller, *Phys. Rev. B Condens. Matter*, 1996, **54**, 11169-11186.

35. G. Kresse and D. Joubert, *Phys. Rev. B*, 1999, **59**, 1758-1775.

36. J. Paier, M. Marsman, K. Hummer, G. Kresse, C. I. Gerber and J. G. Angyan, *J. Chem. Phys.*, 2006, **124**, 154709.

37. M. Gajdoš, K. Hummer, G. Kresse, J. Furthmüller and F. Bechstedt, *Phys. Rev. B*, 2006, **73**, 045112.

38. Y. Hinuma, G. Pizzi, Y. Kumagai, F. Oba and I. Tanaka, *Comput. Mater. Sci.*, 2017, **128**, 140-184.

39. A. Togo and I. Tanaka, *arXiv*, 2018, DOI: 10.48550/arXiv.1808.01590.

40. G. K. H. Madsen, J. Carrete and M. J. Verstraete, *Comput. Phys. Commun.*, 2018, **231**, 140-145.

41. Y. Kumagai, N. Tsunoda, A. Takahashi and F. Oba, *Phys. Rev. Mater.*, 2021, **5**, 123803.

42. J. P. Perdew, A. Ruzsinszky, G. I. Csonka, O. A. Vydrov, G. E. Scuseria, L. A. Constantin, X. Zhou and K. Burke, *Phys. Rev. Lett.*, 2008, **100**, 136406.

43. S. P. Ong, W. D. Richards, A. Jain, G. Hautier, M. Kocher, S. Cholia, D. Gunter, V. L. Chevrier, K. A. Persson and G. Ceder, *Comput. Mater. Sci.*, 2013, **68**, 314-319.

44. N. Tsunoda, Y. Kumagai and F. Oba, *Comput. Mater. Sci.*, 2022, **203**, 111068.

45. C. Freysoldt, B. Grabowski, T. Hickel, J. Neugebauer, G. Kresse, A. Janotti and C. G. Van de Walle, *Rev. Mod. Phys.*, 2014, **86**, 253-305.

46. F. Oba and Y. Kumagai, *Appl. Phys. Express.*, 2018, **11**, 060101.

47. C. Freysoldt, J. Neugebauer and C. G. Van de Walle, *Phys. Rev. Lett.*, 2009, **102**, 016402.

48. Y. Kumagai and F. Oba, *Phys. Rev. B*, 2014, **89**, 195205.
49. R. W. Nunes and X. Gonze, *Phys. Rev. B*, 2001, **63**, 155107.
50. A. Jain, S. P. Ong, G. Hautier, W. Chen, W. D. Richards, S. Dacek, S. Cholia, D. Gunter, D. Skinner, G. Ceder and K. A. Persson, *APL Mater.*, 2013, **1**, 011002.
51. F. Ricci, W. Chen, U. Aydemir, G. J. Snyder, G. M. Rignanese, A. Jain and G. Hautier, *Sci. Data*, 2017, **4**, 170085.
52. S. Kiyohara, D. Mora-Fonz, A. Shluger, Y. Kumagai and F. Oba, *J. Phys. Chem. C*, 2022, **126**, 18833-18838.
53. M. O. Filso, E. Eikeland, J. Zhang, S. R. Madsen and B. B. Iversen, *Dalton Trans.*, 2016, **45**, 3798-3805.
54. S. Del Bucchia, J. C. Jumas and M. Maurin, *Acta Crystallogr. B*, 1981, **37**, 1903-1905.
55. K. Momma and F. Izumi, *J. Appl. Crystallogr.*, 2011, **44**, 1272-1276.
56. J. Vidal, S. Lany, M. d'Avezac, A. Zunger, A. Zakutayev, J. Francis and J. Tate, *Appl. Phys. Lett.*, 2012, **100**, 032104.
57. B. D. Malone, A. Gali and E. Kaxiras, *Phys. Chem. Chem. Phys.*, 2014, **16**, 26176-26183.
58. F. Y. Ran, Z. Xiao, Y. Toda, H. Hiramatsu, H. Hosono and T. Kamiya, *Sci. Rep.*, 2015, **5**, 10428.
59. Y. Kumagai, L. A. Burton, A. Walsh and F. Oba, *Phys. Rev. Appl.*, 2016, **6**, 014009.
60. H. Yanagi, Y. Iguchi, T. Sugiyama, T. Kamiya and H. Hosono, *Appl. Phys. Express.*, 2016, **9**, 051201.
61. C. Yamamoto, X. He, T. Katase, K. Ide, Y. Goto, Y. Mizuguchi, A. Samizo, M. Minohara, S. Ueda, H. Hiramatsu, H. Hosono and T. Kamiya, *Adv. Funct. Mater.*, 2020, **31**, 2008092.
62. S. Byun, B. Ge, H. Song, S. Cho, M. S. Hong, J. Im and I. Chung, *Joule*, 2024, **8**, 1520-1538.
63. G. Domingo, R. S. Itoga and C. R. Kannewurf, *Phys. Rev.*, 1966, **143**, 536-541.
64. K. Kourtakis, J. DiCarlo, R. Kershaw, K. Dwight and A. Wold, *J. Solid State Chem.*, 1988, **76**, 186-191.
65. A. Sanchez-Juarez and A. Ort z, *Semicond. Sci. Technol.*, 2002, **17**, 931-937.
66. R. D. Shannon, *Acta Crystallogr. A.*, 1976, **32**, 751-767.
67. L. Pauling, *Cornell University Press: New York*, 1960, 515.
68. P. Palazzi, *C. R. Acad. Sci. Ser. II.*, 1981, 789.
69. R. Pöttgen and D. Johrendt, *Z. Naturforsch. B*, 2008, **63**, 1135-1148.
70. A. J. Tuxworth, E. E. McCabe, D. G. Free, S. J. Clark and J. S. Evans, *Inorg. Chem.*, 2013, **52**, 2078-2085.
71. S. Bénazeth, M. Guittard and P. Laruelle, *Acta Crystallogr. C*, 1984, **40**, 345-347.

Data availability statement

Crystallographic data for $La_2SnO_2S_3$ has been deposited at the CCDC under CCDC 2322792 and can be obtained free of charge via www.ccdc.cam.ac.uk/data_request/cif, or by emailing data_request@ccdc.cam.ac.uk, or by contacting The Cambridge Crystallographic Data Centre, 12 Union Road, Cambridge CB2 1EZ, UK; fax: +44 1223 336033.